Aerodynamic Performance of Morphing Blades and Rotor Systems

Jürgen Rauleder Technical University of Munich Munich, Germany
Berend G. van der Wall German Aerospace Center (DLR) Braunschweig, Germany
Amine Abdelmoula **Dominik Komp** **Sumeet Kumar** Technical University of Munich, Munich, Germany
Vaclav Ondra **Brano Titurus** **Benjamin K. S. Woods** University of Bristol, Bristol, UK

ABSTRACT

This paper introduces the Shape Adaptive Blades for Rotorcraft Efficiency (SABRE) Horizon 2020 research program and presents initial comprehensive analysis results on the efficacy of adapting blade shapes as a means of reducing rotorcraft power requirements and emissions. The aims of the research program are introduced, followed by discussion of the six different morphing concepts that will be explored. The morphing mechanisms are based on active camber, chord extension, twist, and active tendon morphing technologies. SABRE will explore the use of these concepts individually and in combination, for rotor quasi-steady configuration-type morphing and up to 2/rev actuation of some of the mechanisms, with the objective being to find the best balance between emissions reductions versus complexity and added weight. Initial investigations into the potential power reductions compared to the baseline full-scale BO-105 main rotor achievable with the morphing concepts were performed using Blade Element Momentum Theory and a comprehensive analysis model that was developed using CAMRAD II. The analytical model was validated by full-scale rotor wind tunnel measurements. A combination of active twist and active chord extension achieved up to 11% performance gain in hover. Active camber morphing performance was very sensitive to the combination of deflection, morphing section radial length and placement on the blade, as well as the actuation phasing and blade loading coefficient. The active camber morphing showed power reductions of up to 5.5% in hover and 5% at an advance ratio of 0.313 with a 2/rev actuation, while the active tendon concept showed the capability to change the dynamic response of the rotor blade.

INTRODUCTION

Shape Adaptive Blades for Rotorcraft Efficiency (SABRE) is a 3.5 year long H2020 Research and Innovation Action which will develop helicopter blade morphing technologies with the objective of significantly reducing helicopter fuel burn, CO2 and NOx emissions. The research within SABRE is being performed by a consortium of six partners from four European countries, including DLR and TU Munich in Germany, CIRA in Italy, TU Delft in the Netherlands, and Swansea University and the University of Bristol in the UK.

SABRE will undertake a comprehensive, multidisciplinary research program that aims to remove one of the most fundamental limitations on helicopter performance: the need for rotor blades to have a single fixed geometry, which is inherently a compromise between widely different operating conditions. SABRE envisions shape adaptive blades that can continuously change their shape to optimize performance in rapidly changing aerodynamic environments over the rotor azimuth and changing flow conditions along the blade span, and between different flight states such as hover and fast forward flight. Therefore, the investigated morphing technologies and actuation strategies vary in terms of achievable actuation frequencies and maximum deflections, some of them tailored towards quasi-static actuation (i.e., configuration-type changes, hover versus forward flight), and other investigated mechanisms suited for up to 2/rev actuation to achieve optimum rotor performance.

To investigate the complex research questions, SABRE uses a tightly cross-linked, dual-stream research approach with emissions-focused rotor performance analysis running concurrently with morphing technology development. The analysis stream will combine comprehensive rotor analysis, high-fidelity aerodynamic and structural solvers, detailed

Presented at the AHS International 74th Annual Forum & Technology Display, Phoenix, Arizona, USA, May 14-17, 2018.

morphing mechanism models, and emissions models, creating the most detailed, transdisciplinary, and comprehensive model of its type. The technology development stream will mature a selected group of novel, beyond state-of-the-art, helicopter focused morphing concepts through a carefully considered program of modelling, design, and experimental testing efforts. The analysis stream will guide the development of the morphing technologies towards optimized individual design configurations and combinations of different morphing concepts along the blade, maximizing rotor and fuel efficiency, thus reducing emissions.

With this research strategy and goals in mind, the focus of the current work was on initial performance estimates that can be achieved by one or more of the active morphing technologies in combination, using lower-order aerodynamics and dynamics analysis methodologies. Providing the technology partners with first-order estimates as to the optimum actuation and deflection targets, geometric configurations on the rotor blades and the combination of morphing mechanisms was one further goal of the studies discussed in this paper.

MORPHING TECHNOLOGIES

The six different morphing concepts to be researched allow for active control of some of the primary design parameters which affect the performance of helicopter rotors, namely twist, camber, chord and stiffness (through active tendons). Specific technological approaches for each morphing concept are proposed, and it is foreseen that multiple morphing concepts may be applied to a single blade to create a multi-morphing blade that simultaneously targets multiple physical mechanisms of rotor performance improvement. Actuation systems that can operate in the demanding rotary wing environment are a critical component of rotor morphing, and this project will investigate different actuation technologies capable of delivering the large forces and moments required. Given that the objective of this work is to provide performance increases that can reduce emission, previous research has shown that the actuation bandwidth of interest is quasi-static up to 2/rev (Refs. 1,2). Included in this will be the development of novel passive energy balancing concepts which passively stores energy to offset the actuation requirements of the morphing structures, reducing actuation energy by as much as 90% (Ref. 3).

Active Twist

Directly varying the twist of a rotor blade is a very effective means of varying performance, and this project will pursue two different twist morphing concepts.

Carrying on from work started in the FRIENDCOPTER program (Ref. 4), a Shape Memory Alloy (SMA) driven active twist concept will be pursued. An SMA torque tube will be designed for integration into blade sections in a manner which provides direct elastic twisting of the blade section when actuated. SABRE will represent a significant step forward for this concept through a multidisciplinary, highly integrated design approach (implying the interaction among rotor aeromechanics, advanced aerodynamic prediction techniques, non-linear structural analyses also focusing on the SMA behaviour), system integration (supporting/transmitted structure to be integrated within the blade, actuation, sensing and control; and demonstration at several levels (lab and wind tunnel tests). Different SMA/structural configurations will be initially taken into account and a trade-off will be organised on the basis of dedicated down selection criteria. All the investigated concepts will be characterised by the possibility of inducing a local or distributed torque moment. For illustration purposes, in Figure 1(a) a scheme of a concept based on a SMA tubular element that will be taken into consideration is provided. The use of optical fibres for high resolution, distributed shape sensing will be considered in parallel as an efficient sensing approach applicable to this and other SABRE concepts. A novel inertially driven active twist concept will also be researched within SABRE. This concept, shown in Figure 1(b), actively varies the position of small tip masses to exploit the high centrifugal loads at the blade tip to generate torsional moments.

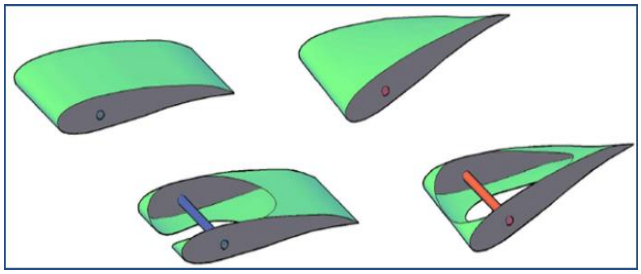

(a)

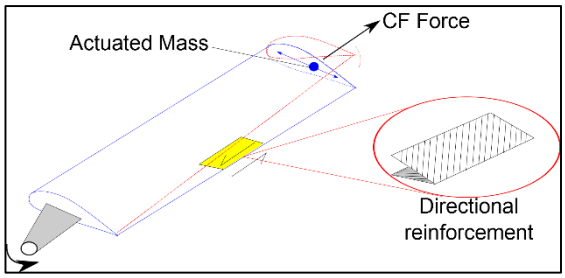

(b)

Figure 1. a) SMA driven active twist concept and b) schematic of inertial twist concept.

These torsional moments can then drive elastic twist of the blade, affecting the resulting blade performance. A change in centrifugal force is obtained by moving a mass near the tip of the blade; with the displacement of the mass perpendicular to the radial direction. Extension-shear coupling is introduced into the blade (through composite stiffness tailoring). This coupling converts the changing axial centrifugal forces into torsional pitching moments, which act between the blade tip and root, elastically twisting the entire blade inboard of the device. This novel concept takes advantage of the large

centrifugal accelerations towards the tip of the blade and is able to affect a significantly larger portion of the blade than in which it is located.

Active Camber

Actively varying the amount of camber present in an aerofoil is an effective means of changing the lift and pitching moment created by a blade section. This can be used to significantly influence rotor performance in two different ways: via direct changes in thrust or via the servo effect, where camber-induced pitching moments are used to elastically twist the portion of the blade inboard of the morphing camber section. Camber variation is arguably the most successful approach used in active rotor research to date (e.g. the Boeing SMART rotor and Airbus Helicopters Blue Pulse), although this has mostly taken the form of discrete trailing edge flaps, and the control authority achieved to date has been insufficient for significant performance improvements.

SABRE will develop two promising continuous, compliance-based camber morphing technologies. The first is the Fish Bone Active Camber (FishBAC) morphing airfoil concept, which has shown excellent performance under initial development (Ref. 5). This concept, shown in Figure 2(a), combines a compliant internal spine and rib structure with an elastomeric matrix composite (EMC) skin surface. An antagonistic tendon system drives large magnitude changes in airfoil camber in a smooth and continuous manner, leading to a very large control authority over airfoil lift ($\Delta C_l > 1.5$) and pitching moment with minimal drag. Wind tunnel testing has shown an increase in lift-to-drag ratio of more than 20% compared to trailing edge flaps (Ref. 6).

The second active camber concept (Figure 2(b)) is the TRanslation Induced Camber (TRIC). Here, a discontinuous lower skin on the trailing edge of the airfoil is translated chordwise via actuation inputs on either end of the surface to induce changes in camber. TRIC has the significant benefit that only bending is required in the skin to morph (and not extension), which allows for the use of high strength polymer matrix composite materials. Another advantage of this approach is its versatility, as synchronous actuation produces pure camber change while asynchronous actuation induces twist through the warp twist effect (Ref. 7).

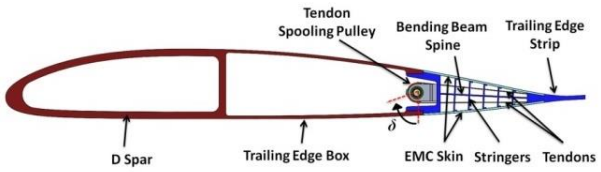

(a)

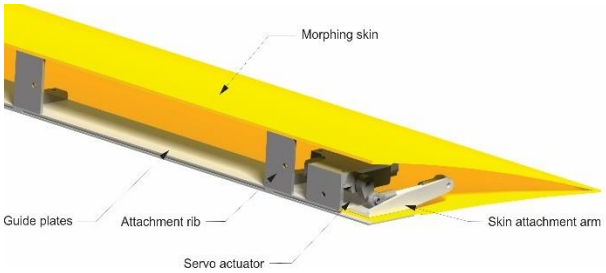

(b)

Figure 2. Active camber concepts a) FishBAC morphing airfoil and b) Translation Induced Camber.

Both the FishBAC and TRIC concepts have a significant advantage over other active camber concepts in that they can be used to create pure camber change or differential camber change (through differential actuation of the ends of the surface) – effectively creating blade twist.

Chord Extension

Chord Extension for increased blade area has been proposed in the literature, typically by sliding a discrete chord extension plate out of the trailing edge. However, this approach does not create a smooth aerofoil shape, and therefore incurs significant drag penalties. This project will instead investigate a more aerodynamic and structurally integrated approach, known as Variable Chord Extension wherein a portion of the trailing edge of the blade is hinged outboard such that it may fan out on a set of sliding rails to provide a linear increase in chord over the morphing region, as seen in Figure 3. An internal low-density, zero-Poisson's ratio cellular core (Ref. 8) extends with the trailing edge and the core is covered with either an elastic or rigid sliding skin. This approach provides a significantly more aerodynamic deformed shape than a discrete section of chord morphing because it does not create a sharp discontinuity in the blade surface, significantly reducing the drag penalty. Furthermore, the outboard hinge provides a simple and robust mechanism to transfer the significant centrifugal loads acting on the trailing edge into the primary blade structure. Chord extension in this way allows for better approximation of the ideal chord distributions for both hover and forward flight.

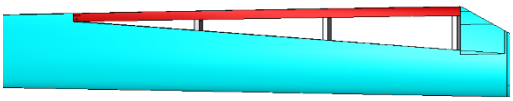

(a)

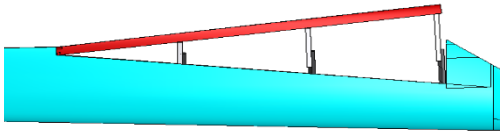

(b)

Figure 3. Variable chord extension concept, a) retracted, and b) deployed.

Active Tendons

Tendons – structural components loaded axially in tension – are used widely in mechanical and civil engineering to transfer loads across structures, to deliver control action or to improve performance. Tendons with actively variable tension, so called active tendons, embedded in the blade spars (Figure 4) will be used to produce dynamic softening and blade-tendon coupling in centrifugally stiffened blades. Such approach was previously considered only in non-rotating aerospace structures (Ref. 9) and for resonance avoidance in spinning shafts during their spin-up and run-down (Ref. 10). The associated effective blade stiffness reduction will lead to a range of quasi-static and dynamics effects (Ref. 11). These effects will be studied, and additional opportunities will be sought to control the blades. For instance, in terms of their steady state responses under given operational conditions. Advanced interactions through dynamic blade-tendon coupling (Ref. 12) will be studied for possible use as an adaptive Tuned Blade Vibration Absorber. The tendon-based structural control works well within the rotating frame as the actuation element can be placed in the root of the blade, where there is more volume available and where the centrifugal loads are lower.

Active tendons add an important control variable to the shape adaptive rotor system by providing modification of its dynamic response. This can be used to increase the magnitude of blade response to specific morphing inputs (reducing actuation requirements) or to mitigate any undesired dynamic characteristics introduced by alterations to the baseline blade structure.

Passive Energy Balance

One of the novel aspects of SABRE is the consideration from the very beginning of the project of means to reduce actuation requirements. Historically, actuation has been one of the most challenging aspects of active rotor systems, but recent work has shown that actuation requirements can be drastically reduced (leading to smaller, lighter, and lower power actuators) if portions of the energy required for deformation can be provided through passive energy balancing in both a quasi-static and dynamic sense.

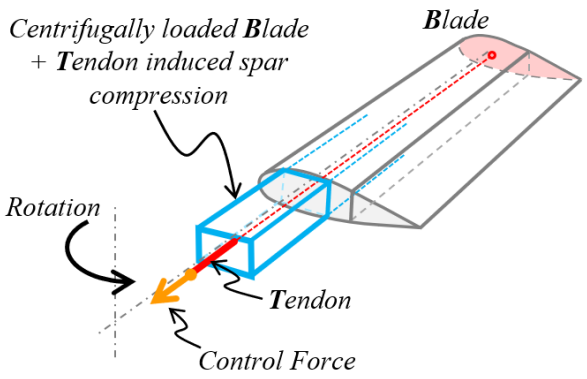

Figure 4. Active tendon concept.

SABRE will achieve quasi-static passive energy balancing by applying the Spiral Pulley Negative Stiffness (SPNS) mechanism in the rotating field for the first time. The operating principle behind this concept is shown in Figure 5. This device uses a pulley with an optimized spiral shape to convert the decreasing force available from a pre-tensioned linear drive spring into an increasing torque available – effectively creating negative torsional stiffness. Experiments and analysis have shown the ability of the SPNS device to reduce actuation torque requirements by 92% and energy by 90% (Ref. 3). Other options for quasi-static passive energy balancing will be considered, such as pre-stressed deformable members (*e.g.* pre-buckled columns) integrated into the structure. In addition to developing refined designs for such mechanisms, the work will develop a mass optimization strategy that balances savings in actuator weight with any additional weight incurred by the negative stiffness mechanism. Resonant actuation will provide dynamic passive energy balancing, at frequencies up to the target maximum of 2/rev.

The aim is to minimize the forces and energies required to affect these higher speed morphing deformations by ensuring that the required deformation coincides with a resonance at the frequency required. It has been shown that the addition of negative stiffness through the use of bi-stable plates can reduce the natural frequency of a structure for the purpose of vibration isolation; a similar principle could be applied here to reduce the natural frequency of a morphing mechanism to a harmonic of the rotor speed. The quasi-static negative stiffness concepts such as the SPNS device and pre-stressed members will also be evaluated for their performance at higher frequencies. In the latter case, the amount of pre-stress could be controlled using smart materials, allowing a degree of semi-active control of natural frequency variation in response to environmental changes.

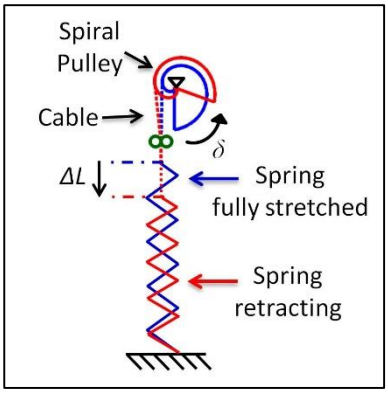

(a)

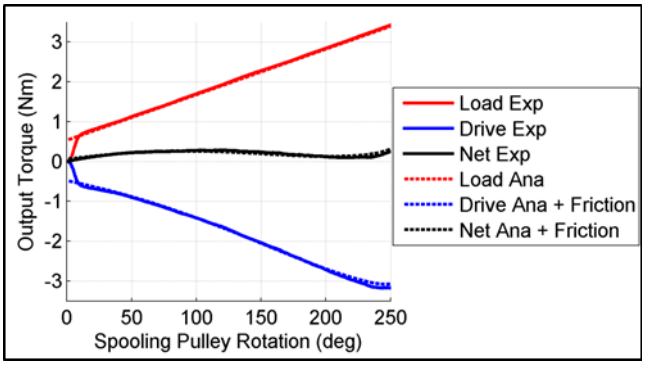

(b)

Figure 5. Spiral Pulley Negative Stiffness a) concept schematic and b) experimental (Exp) measurements and analytical (Ana) predictions (Ref. 3).

MULTI-MORPHING ROTOR

In addition to the six individual morphing concepts listed above, SABRE will also investigate the use of multiple concepts on a single rotor blade, to allow for simultaneous targeting of multiple different methods of reducing power requirements and therefore emissions. In addition to combinations of the geometry changing mechanisms discussed above, the Passive Energy Balancing and Active Tendon concepts are particularly well suited to be used within a multi-morphing rotor system, as they allow for reductions in the actuation energy requirements and for tuning of the dynamic response of the blade, directly addressing two of the primary concerns of multiple morphing mechanisms: excessive actuation energy/power requirements and dynamic interference. Figure 6 shows one such possible combination of multiple concepts, although this is just an initial notional schematic. The design and optimization of such a rotor system is a complex, multi-disciplinary task, and the goal of the SABRE program is to provide initial results as to what might be a promising approach to the specific problem of emissions reductions, and to develop the underlying morphing technologies required.

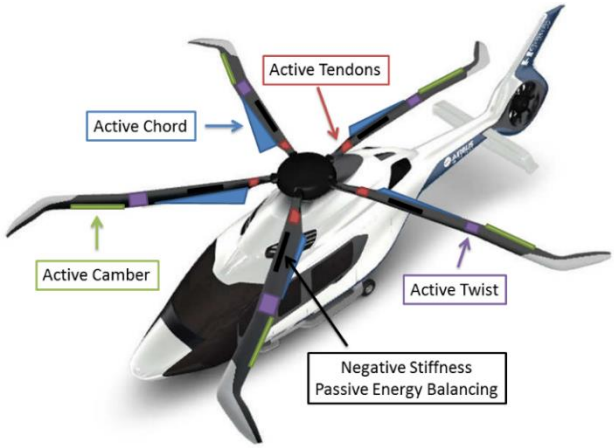

Figure 6. Multi-morphing rotor concept.

BLADE ELEMENT MOMENTUM THEORY INVESTIGATIONS

One potentially promising multi-morphing rotor configuration is the combination of twist and chord morphing – as it allows the rotor to approach as close as possible the "optimum hovering rotor" described in the classical literature which has the best possible figure of merit, FM. This is achieved first by minimizing the induced power to as close as possible to the ideal power of a constant inflow distribution. The second step is minimizing the airfoil profile power via the best possible lift-to-drag ratio distribution along the span to obtain best possible airfoil efficiency. The textbook solution of this optimum hovering rotor includes a hyperbolic twist and a hyperbolic chord distribution along span, however, by ignoring blade tip and root losses, root cutout, compressibility and stall. The morphing investigated is shown in Figure 7.

To initially investigate potential performance gains of the rotor system, blade element momentum theory (BEMT) was used with realistic approximations of airfoil coefficients including compressibility, stall, and blade root and tip losses.

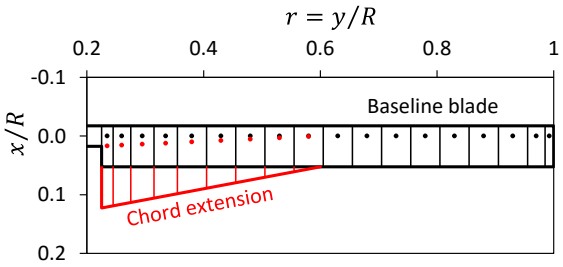

(a) Chord morphing to approximate hyperbolic chord distribution.

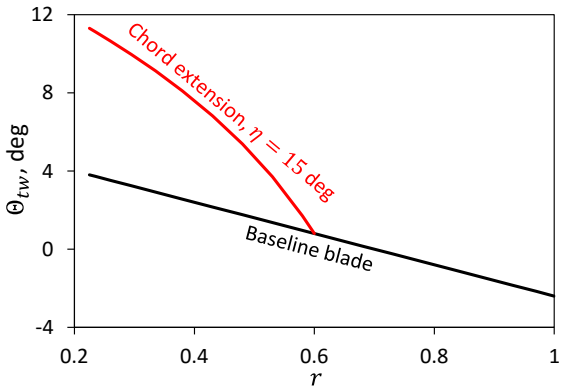

(b) Aerodynamic twist morphing by deflection of chord extension to approximate hyperbolic twist distribution.

Figure 7. Chord extension with deflection for improvement of hover FM.

Evaluated was the potential of twist morphing, chord morphing with and without deflection of the chord extension, and combinations of all with respect to maximizing the hover FM. Results were computed assuming rigid rotor blades and the hovering rotor condition of the BO-105 main rotor was investigated. The chord deployment may be inclined similar to a flap, which modifies the chord line orientation and hence the aerodynamic blade twist. The latter comes with an addition to morphing the overall blade twist. The baseline blade section solidity is σ_{BL} = 0.07. The solidity and the aerodynamic (elastic) twist introduced by deflecting the deployed part of the chord in the morphed region are defined by

$$\sigma(r) = \sigma_{BL} + \Delta\sigma \frac{r_\sigma - r}{r_\sigma - r_a}$$
$$\Delta\Theta_{tw} = \tan^{-1} \frac{\Delta\sigma \sin\eta}{\sigma_{BL} - \Delta\sigma \cos\eta} \qquad (1.1)$$

Therein, r_σ is the radial position of the chord morphing hinge and η is the deflection angle. This is illustrated in Figure 8.

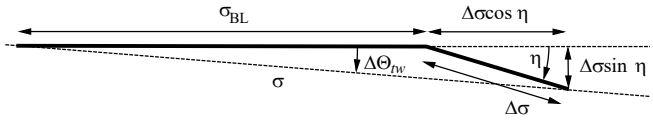

Figure 8. Chord extension with deflection.

The reference main rotor thrust for a 2200 kg BO-105 helicopter plus an estimated 50 kg aerodynamic download of the fuselage due to the main rotor downwash was used, resulting in a thrust of T = 22,073 N, or a thrust coefficient of C_T = 0.005, giving a blade loading coefficient of C_T/σ_{BL} = 0.0714. The following simplifications were applied: no precone of the blades, no rigid or elastic blade motion in flap or lag, and no rigid or elastic blade torsion. Therefore, aerodynamic moments about the quarter chord, or a variation of the aerodynamic axis relative to the elastic axis, are not considered here. However, realistic airfoil polars in lift and drag coefficients were used, that include compressibility and stall, depending on Mach number, as shown in Figures 9(a) and (b), while in (c) the resulting lift-to-drag ratio is given. The analytical model used in the study is sufficiently well representing the tabulated data (thick lines) from wind tunnel measurements.

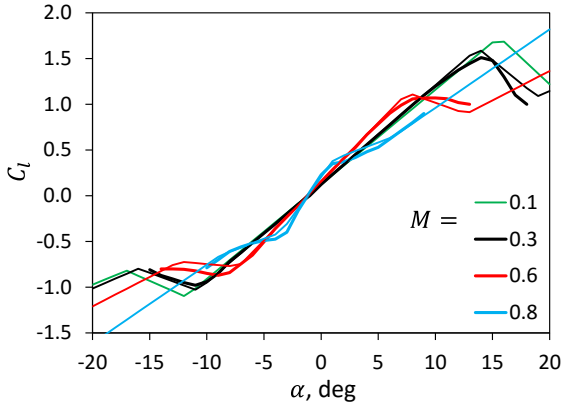

(a) Lift coefficient

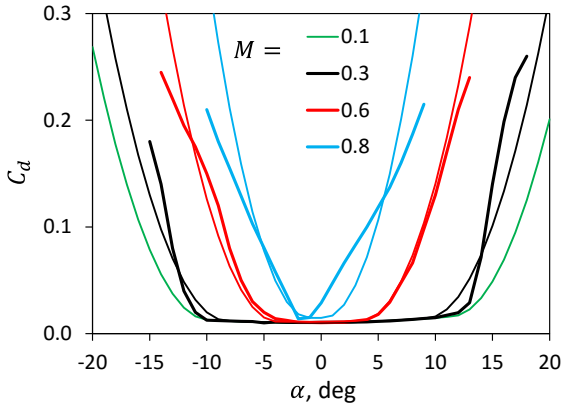

(b) Drag coefficient

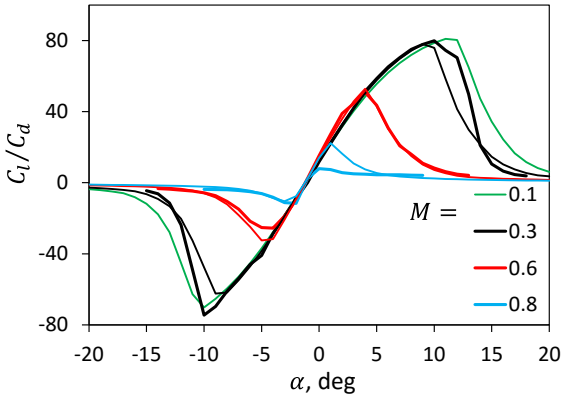

(c) Airfoil lift-to-drag ratio

Figure 9. Airfoil characteristics of tabulated wind tunnel data (thick lines) and analytical synthesis (thin lines).

Blade tip losses are accounted for by using Betz' formula for both the blade tip and the root of the blade. Results for the hover FM are obtained for a large range of rotor thrust values from zero up to maximum thrust in deep stall. For a given thrust value, the collective control was varied systematically in an outer loop, while in an inner loop the local lift and local induced inflow were iterated until convergence was obtained. This was performed for the overall blade twist morphing, for the chord morphing, for the deflected chord morphing, and for combining all together. In addition, all computations were performed with and without root and tip losses to get an impression of their respective influence.

Results obtained for twist morphing are shown in Figure 10, confirming textbook conclusions that a high amount of overall blade twist and a high rotor loading are required for the largest possible FM. Only in vicinity of stall the FM including tip losses is better than that without losses, because they reduce the effective section angle of attack especially in the root and tip region, alleviating stall there, thus reducing airfoil drag and rotor power.

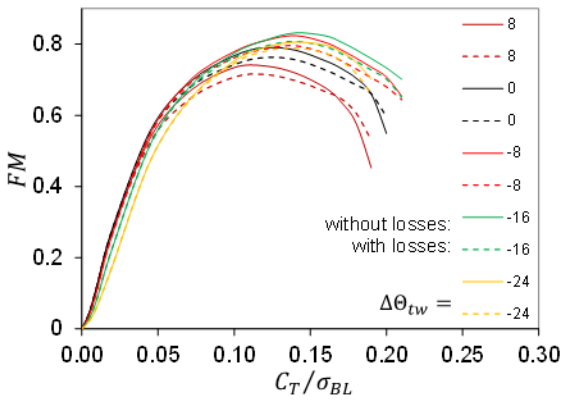

Figure 10. FM of the baseline rotor with twist morphing without tip losses (solid lines) and including tip losses (dashed lines).

At the nominal rotor blade loading coefficient of C_T/σ_{BL} = 0.0714 the best FM is obtained with $\Delta\Theta_{tw}$ = -8 deg/R of additional twist (i.e., the total twist was -16 deg/R in this case), although the result was very close to $\Delta\Theta_{tw}$ = 0 deg/R, which represents the original unmorphed rotor with its built-in twist of -8 deg/R. The highest achievable overall thrust was obtained with a high amount of additional twist (-16 deg/R). Less twist yielded more stall at the blade tip, and more twist yielded deeper stall at the inboard blade sections. Combining chord and twist morphing is shown in Figure 11 for 100% chord deployment at the root and a hinge position at 60% of the rotor radius. The airfoil aerodynamic coefficients remain unaffected, although a chord extension – without thickening the airfoil in the same proportion – generates thinner airfoils that must be suspected to have different characteristics. Inclusions of such modifications are focus of a later stage of the SABRE project.

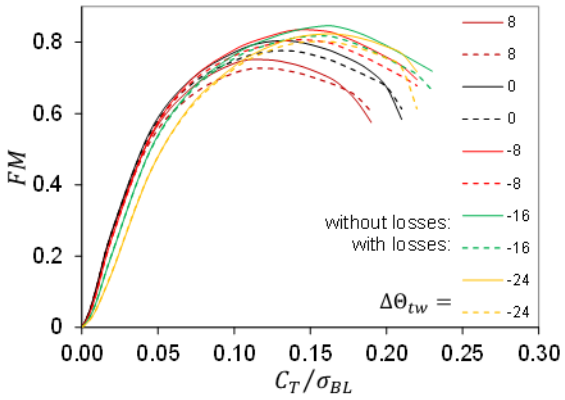

Figure 11. FM with 100% chord and twist morphing.

In addition to the undeflected chord morphing, the deployed part may be deflected by some angle as shown in Figure 8. The entire range of thrust from zero to maximum for various additional twist is shown in Figure 12.

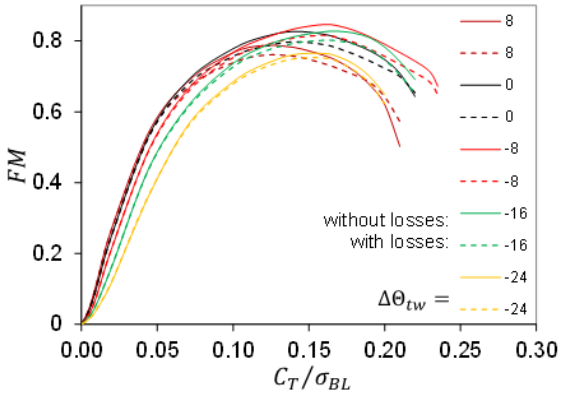

Figure 12. FM with 100% chord, 15 deg deflected, and twist morphing.

In practically all conditions the inclusion of root and tip losses has a figure of merit less than without these losses. The highest FM achievable is obtained now with 100% chord morphing, η = 15 deg deflected, and an additional twist of $\Delta\Theta_{tw}$ = -8 deg/R, which is much less than for the chord extension only. The reason is that with a deflected chord extension additional twist introduced in the inner part of the blade, more closely resembling a hyperbolic twist.

Compared to all twist and chord morphing outlined before the optimum hovering rotor should provide the best figure of merit all over, but theoretically it should also employ an adaptation of the tip solidity for every thrust, in order to operate at the best lift-to-drag ratio possible at every thrust value. For small thrust this would lead to very small chord lengths, while for large thrust the chord length would increase. Under such conditions the Figure of Merit would be more than 0.8 at every thrust value. It must also be kept in mind that the definition of the "optimum hovering rotor" stems from incompressible flow assumption without stall, while here compressible flow and stall are applied, and the

definition also excludes root and tip losses, while here they are also included. For comparison only the Figure of Merit and power gains of this "optimum hovering rotor" are also indicated in the following section graphs as circle mark at zero additional twist. At nominal thrust the optimum hovering rotor is always performing better than all chord and twist morphing variations, but at high thrust it is partly superseded by chord and twist morphing, because the chord length of the optimum hovering rotor is not further adapted.

Results were also obtained for 50% chord deployment, 7.5 and 15 deg deflection, and for different radial chord hinge positions. From all these results the optimum combination could be selected for the nominal thrust and for a high thrust condition. For the nominal rotor thrust and 60% hinge position the biggest gains can be obtained by twisting alone (see Figure 13) but it requires $\Delta\Theta_{tw}$ = -8 deg/R additional twist. The second largest gains are obtained with a 50% chord extension deflected by η = 7.5 deg, which requires only $\Delta\Theta_{tw}$ = -4 deg/R additional twist; and the undeflected chord extension of 50%, but again $\Delta\Theta_{tw}$ = -7 deg/R additional twist are needed there.

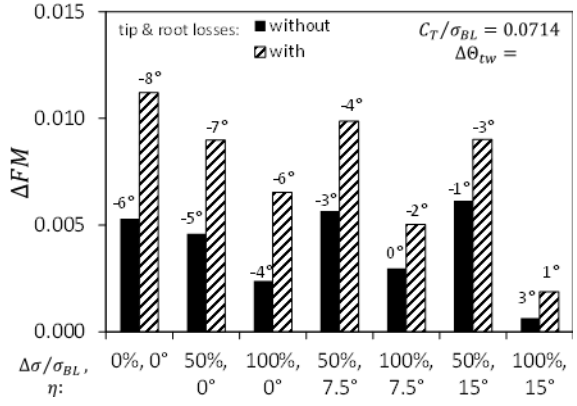

(a) FM for varying blade twist, chord, and deflection

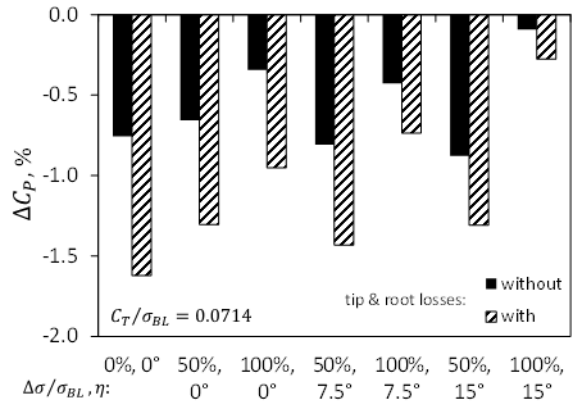

(b) Rotor power for varying blade twist, chord, deflection

Figure 13. Gains in FM and rotor power relative to the baseline blade, nominal thrust, 0.6R hinge position.

At a higher thrust level of C_T/σ = 0.16 and again the morphing concept results are compared relative to the performance of the baseline rotor. Results are given in Figure 14. Here the achievable gains are much larger than at the design thrust, and the maximum gains achievable now are obtained for 100% chord morphing with a deflection of η = 7.5 deg, closely followed by 100% chord morphing without a deflection. A chord morphing of 50% is still rather close to the 100% morphing, now a deflection results in little higher gains than without. The gains are significantly larger than at the design point of the blade, because the morphing with a larger blade area allows for larger thrust with less control angle, thus more margin relative to stall and the smaller angles of attack also reduce the profile drag. All optimum points require more additional twist morphing of the blade than at design thrust, which is caused by the high loading.

Finally, the power gains are provided in Figure 14(b) and gains up to 11% were achieved with and without considering losses. Same as for FM, the 100% chord morphing without and with deflection was best, closely followed by the 50% chord morphing, and little below the twist morphing alone. The chord morphing hinge position was also varied with all combinations outlined before. Taking into account all of the discussed variations, the most promising combinations of morphing parameters can be summarized as follows.

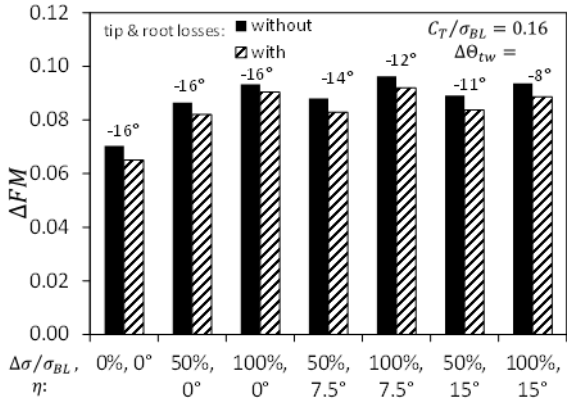

(a) FM for varying blade twist, chord, and deflection

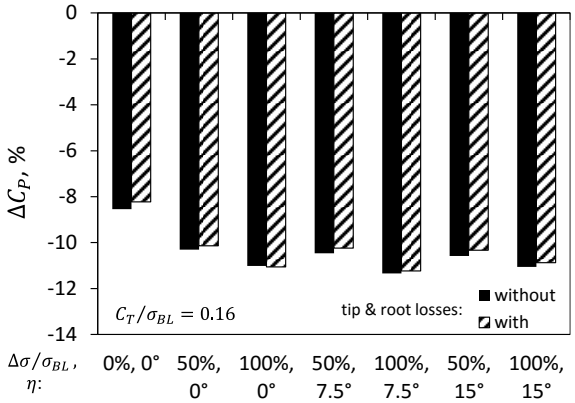

(b) Rotor power for varying blade twist, chord, deflection

Figure 14. Gains in FM and rotor power relative to the baseline blade. High thrust, 0.6R hinge position.

Nominal thrust, C_T/σ = 0.0714: BL rotor data are FM = 0.680, C_P = 0.000367. Twist morphing alone can already

provide close to the largest gains achievable, and only little more can be achieved with 50% chord morphing and a moderate deflection of the extended section of the blade by 7.5 deg. The innermost hinge position of 40% radius was found to be superior to the others.

High thrust, C_T/σ = 0.16: BL rotor data are FM = 0.727, C_P = 0.001152. In this case, 100% chord morphing could significantly improve the Figure of Merit. The outermost hinge position at 60% radius was needed, combined with a moderate deflection of the extended chord section of 7.5 deg to achieve the optimum performance.

CAMBER MORPHING STUDIES

The full-scale BO-105 hingeless rotor was used as the baseline to analyze performance gains accrued using the camber morphing mechanism detailed earlier. The comprehensive analysis tool CAMRAD II was used for this purpose (Ref. 13). The main rotor structural properties for the BO-105 main rotor were provided by DLR, and in the initial stage of the modeling efforts these structural properties were assumed unchanged for the morphed sections and radial stations. General characteristics of the rotor are listed in Table 1.

Table 1. BO-105 main rotor parameters

Rotor type	Hingeless
Number of blades, N_b	4
Radius, R	4.91 m
Airfoil cross section	NACA23012
Solidity, σ	0.07
Rotor blade tip speed	218.1 m/s
Blade twist (root to tip)	-8 deg (linear)

Computational efficiency is important, because many combinations of morphing mechanisms on the blades need to be investigated, along with various actuation strategies and deflection targets to enable a performance and efficiency optimization of the rotor system. Therefore, the blade aerodynamics model was based on lifting line theory that used aerodynamic properties of two-dimensional airfoil sections (lift, drag and pitching moment) organized in a C81 table look-up form, and the highest level of fidelity that was used for the wake model was a free vortex wake formulation. Aerodynamically, the camber morphed shapes of the rotor blades were represented in the comprehensive analysis model by using modified airfoil tables. Unlike for standard (non-morphing) rotors, these airfoil tables are changed not only based on the aerodynamic conditions such as local Mach number, but they are also changed when a deflection of the morphing airfoil sections on the rotor blade occurs, based on the pre-calculated airfoil characteristics as a function of blade or airfoil deflection.

The used C81 table format has an organized layout of the airfoil properties for discrete angles of attack ranging from -180 deg to 180 deg and for a Mach number range of 0 to 1.0. The airfoil tables for the baseline airfoil (NACA23012), as well as the (deflected) camber morphed shapes, were generated using computational fluid dynamics (CFD). These 2-D airfoil aerodynamics results were validated using available wind tunnel measurement data and, in cases were measurements were not available, verified by results obtained using another analysis method, namely XFOIL (Ref. 14).

CFD Study of Camber Morphed Airfoil Sections

A computational aerodynamics study was carried out with the objective of defining morphed camber airfoil shapes based on the airfoil NACA23012 (without tab) and assessing their 2-D performance using the DLR CFD code for compressible flow, TAU. Starting from the leading edge to 75% chord length these generic shapes have the same contour as the baseline case NACA23012. A MATLAB code package provided by University of Bristol was used to morph the camber of the baseline profile, over the aft quarter chord, and generate new airfoil shapes for further investigation. It used a third order polynomial shape function to define the new camber based on prescribed trailing-edge tip deflections as a percentage of the baseline chord. The shape function was defined only up to 95% chord, acknowledging the practical limitation of affecting camber change close to the trailing edge. Information regarding the analytical expressions used to define the camber morphing is detailed in Ref. 15. Only the aft quarter chord was morphed, because previous investigations showed that this was the aerodynamically most efficient, while still structurally viable geometry. For these reasons, the chordwise morphing section was limited from 75% to 95% chord length, *c*. Different cambered airfoil shapes were generated based on the amount of trailing-edge tip deflection from the baseline.

The following cases of non-dimensional trailing-edge tip deflections were considered – two negative morphed camber cases, NMCC, with negative trailing edge tip deflections of -4% (NMCC2) and -2% deflection (NMCC1) and four morphed camber cases with positive downwards tip deflections 1% (MCC05), 2% (MCC1), 4% (MCC2), 6% (MCC3) and 8% (MCC4). The corresponding airfoil profiles are illustrated in Figure 15. (Please note that the aspect ratio of the inset image is not same as that of the larger image of the complete airfoil sections.) The CFD simulations were conducted over a range of Mach number, *M* between 0.2 and 0.8 and angle of attack, α between -5 and 18 deg. The Reynolds-averaged Navier-Stokes (RANS) equations were solved using a steady RANS solver. However, for certain cases, such as for high angles of attack where the flow became unsteady, a transient solver was used (Unsteady RANS). The generic airfoil shapes were placed in the center of this domain

and the airfoil surface was considered as a viscous wall. The flow was assumed to be fully turbulent.

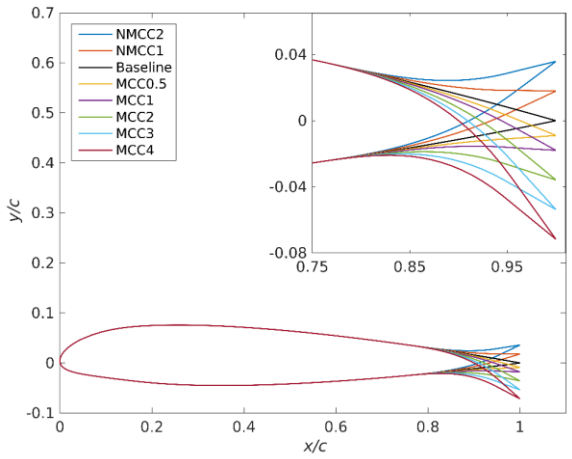

Figure 15. Morphed camber airfoil sections.

The dimensionless wall distance, y^+, was less than 1 for all cases and the cell growth rate corresponded to 1.1. The entire computational domain was built based on a structured mesh. Here, the O-grid block strategy was applied to the boundary layer domain as well as the far field region. This strategy was adopted for the baseline case as well as for the morphed camber cases. The computational domain was bound by a circular boundary with a radius of 50*c*. The backward Euler scheme was used for the time discretization and a central scheme was chosen for the spatial discretization. For the high Mach number study, M=0.8, an upwind scheme was used for spatial discretization. The two-equation Menter SST turbulence model was used to approximate the Reynolds stresses.

A grid convergence study (not shown here) was conducted using different grid resolutions for the baseline case and the most deflected case (MCC4) at M=0.3 and α=0 deg. The medium grid (~95000 cells) was selected for further investigations, since the investigation based on the medium and fine resolution (~190,000 cells) predicted almost the same C_l and C_d distribution over α for the baseline and MCC4 profiles.

The CFD results generated using the above numerical strategy are compared to DLR measurement data for the full scale BO-105 main rotor blade profile in Figure 16 for Mach numbers 0.4, 0.5 and 0.6. Here, the most important flow characteristics such as the linear region of C_l as well as the stall region were numerically well predicted, thereby establishing confidence for further investigations.

Due to lack of available experimental data for the entire spectrum of Mach numbers and angles of attack of interest, a verification of CFD results was carried out by comparison with results obtained using XFOIL. XFOIL is designed to solve inviscid and viscous incompressible flow. Therefore, the range of Mach numbers was limited to M between 0.2 and 0.4.

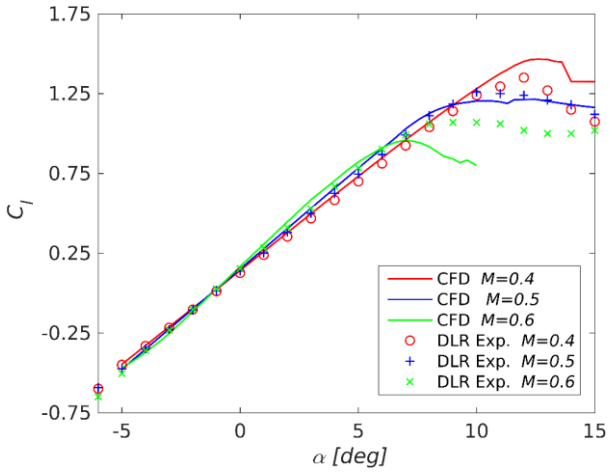

(a) Validation of C_l over α

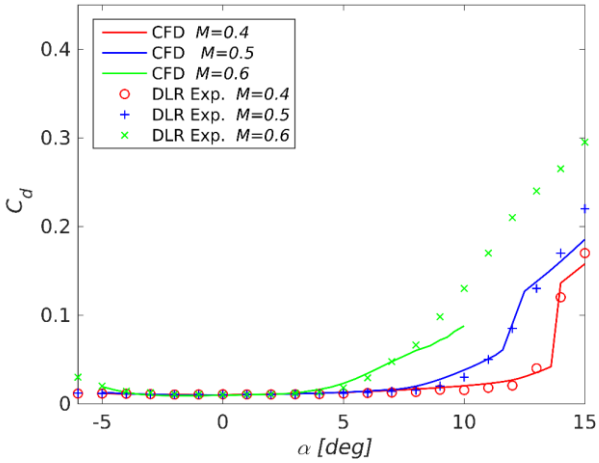

(b) Validation of C_d over α

Figure 16. Validation of NACA23012 CFD results with DLR measurements for different Mach numbers.

For all XFOIL computations the flow was forced to trip from laminar to turbulent at a point very close to the leading edge and the N factor for the transition prediction using the built-in e^N method was set to 9. Figures 17 and 18 show good agreement between CFD and XFOIL results for cambered profiles MCC1 and MCC3, respectively. Both approaches calculated the same slopes of the linear region for the C_l distribution while XFOIL approximated lower drag coefficients for all cases. In the stall region, that is generally to predict, both numerical investigations varied from each other in C_l prediction, since this critical region is difficult to approximate.

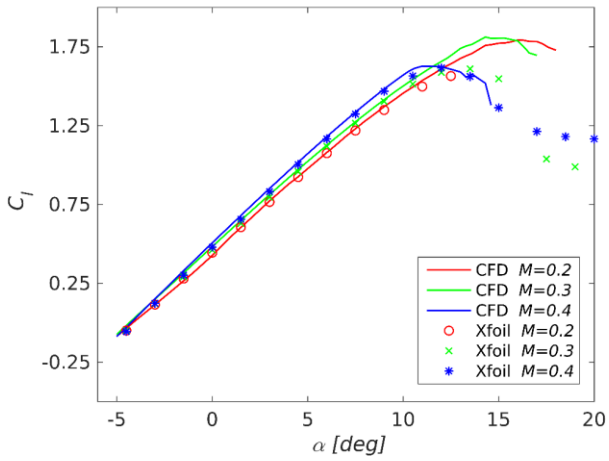

(a) Verification of C_l over α

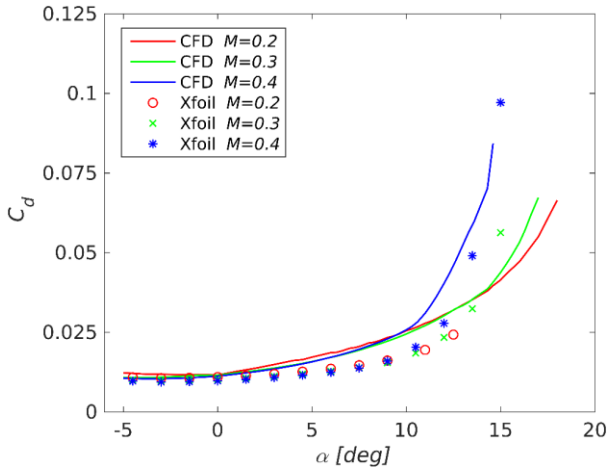

(b) Verification of C_d over α

Figure 17. Comparison of airfoil polars for MCC1 obtained using XFOIL to those predicted by CFD.

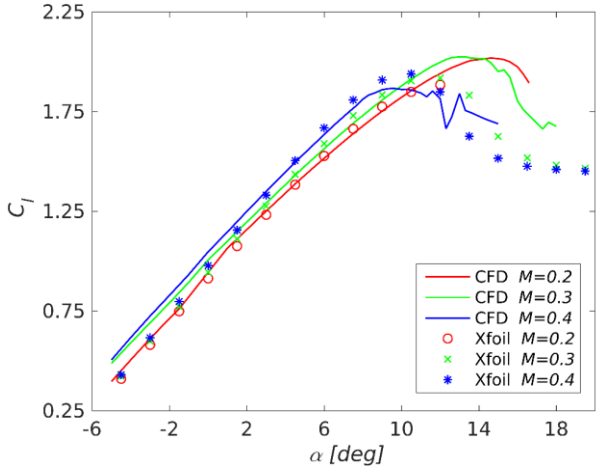

(a) Verification of C_l over α

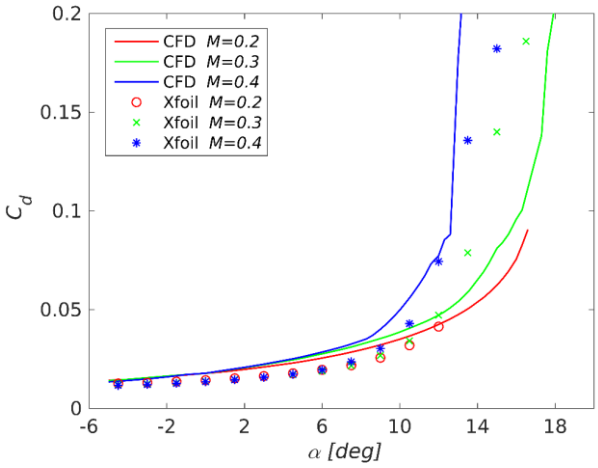

(b) Verification of C_d over α

Figure 18. Comparison of airfoil polars for MCC3 obtained using XFOIL to those predicted by CFD.

Figure 19(a) shows C_l over α distribution for the different morphed camber airfoils at M=0.3. The zero angle of attack corresponds to the horizontal freestream vector for all cases. An increase in camber leads to higher maximum lift coefficient and lift curve slope, and lower airfoil stall angle. NMCC1 and NMCC2 lead to a reduction of C_l over the complete investigated range of angle of attack. For a given angle of attack, the gain in C_l between adjacent profiles decreases with increasing camber. As a result, the largest gain occurs between the baseline profile and MCC1, and it is the lowest between MCC3 and MCC4. Figure 19(b) shows that these lift gains are accrued at the expense of drag. The lower camber morphed cases MCC0.5 and MCC1 showed the lowest drag. MCC3 and MCC4 provided the highest drag penalty, especially in the stall region. The negative deflected shapes showed lower drag for positive angles of attack and increased drag for negative angles of attack.

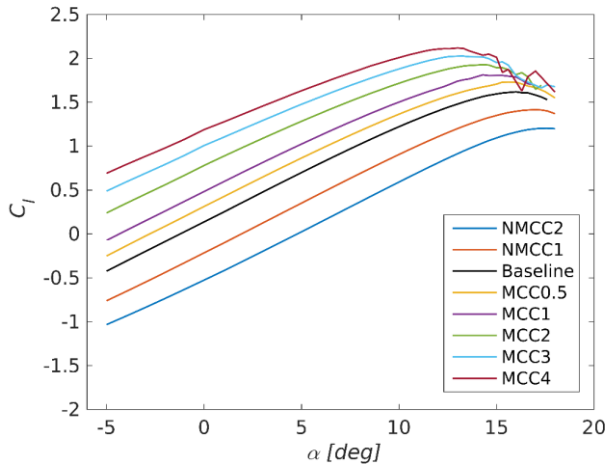

(a) C_l over α for the morphed shapes in comparison to the baseline airfoil

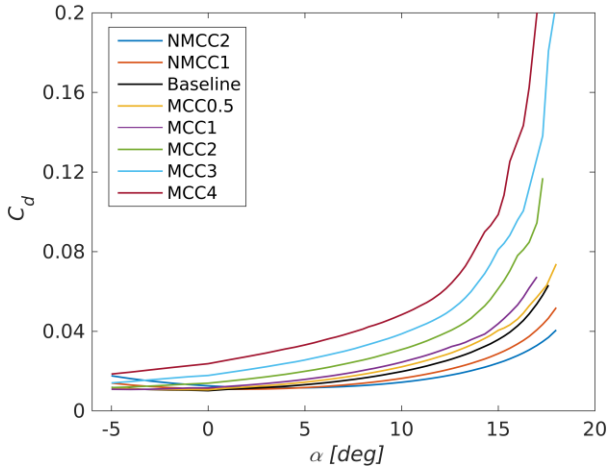

(b) C_d over α for the morphed shapes in comparison to the baseline airfoil

Figure 19. Morphed camber shape airfoil polars obtained using CFD for M=0.3.

In order to quantify the aerodynamic efficiency gains from camber morphing, the lift-to-drag ratio C_l/C_d, is plotted in Figure 20 for M=0.3. As can be seen in Figure 20(a), morphed shapes showed higher C_l/C_d compared to the baseline for α between −5 and 9.6 deg. Figure 20(b) indicates that all of the morphed shapes exhibited the same aerodynamic efficiency for constant C_l in the range between -0.1 and 0.75. Beyond this, MCC0.5, MCC1 and MCC2 showed better efficiency than the baseline. Globally, MCC1 showed the highest C_l/C_d, which was observed for approximately C_l =1.2, where it showed an improvement of about 6% over the baseline. For higher C_l this improvement increased further. The negative deflected cases did not show any improvement in C_l / C_d.

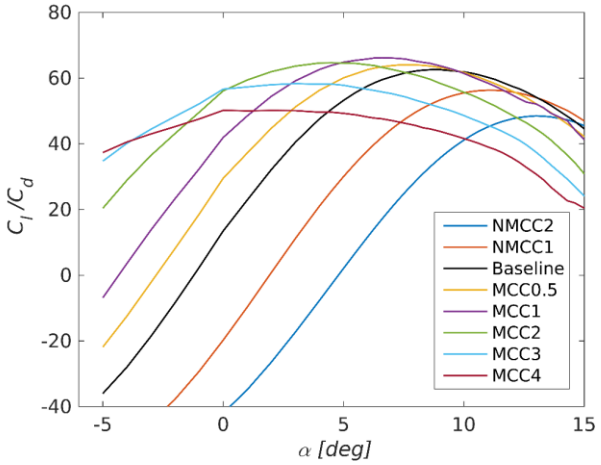

(a) C_l / C_d over α for the morphed shapes in comparison to the baseline airfoil

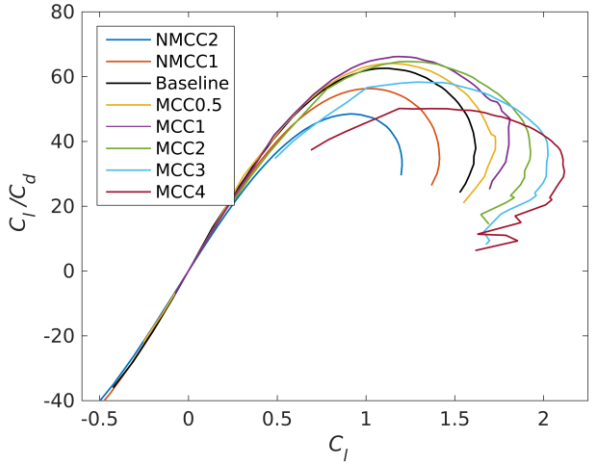

(b) C_l / C_d over C_l for the morphed shapes in comparison to the baseline airfoil

Figure 20. C_l / C_d prediction using CFD for M=0.3.

Comprehensive Analysis of Camber Morphing

A CAMRAD II model was developed using the measured structural and inertial properties of the full-scale BO-105 rotor. The baseline (isolated) rotor structural model is an exact resemblance of the BO-105 main rotor using a NACA 23012 airfoil section throughout. The rotor was modeled using 20 aerodynamic panels and 13 structural elastic beam elements along the blade span. Calculations were carried out over 48 azimuthal stations per revolution. The rotating-blade natural frequencies predicted by the CAMRAD (CII) blade structural model were validated (see Figure 21) by the BO-105 main rotor blade natural frequencies provided by DLR that were previously calculated (Ref. 17) using an FEM code and validated against measurements. All modes were predicted well for the entire spectrum of rotational frequencies, although the 1st torsional and the 2nd lag modes showed a slight divergence for very low rotational frequencies below 20% of the nominal rotational frequency. This divergence will be investigated further. However, since all studies will be conducted at the nominal operating range of the full-scale BO-105 rotor, the slight difference predicted for very low frequencies in 1st torsion and 2nd lag modes is not expected to have significant effects on the results.

The analytical model was further validated by experimental data from extensive hover and forward flight tests of the full-scale BO-105 rotor in the NASA Ames 40-by-80-ft wind tunnel (Refs. 18, 19). For both hover and forward flight validation, the rotor was trimmed using a zero-flapping condition, i.e., the same trim condition as used in the experimental studies.

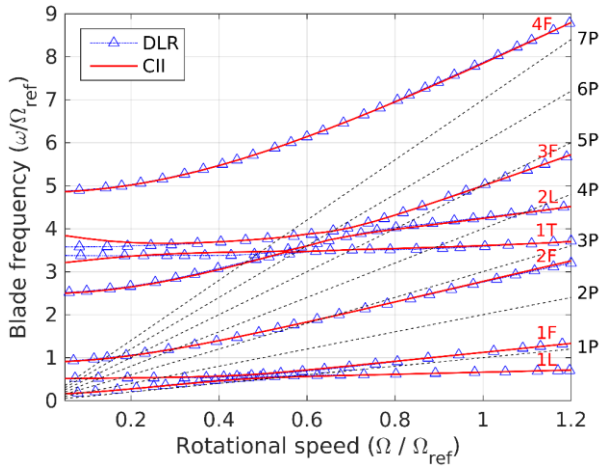

Figure 21. BO-105 main rotor blade natural frequencies.

Figure 22 shows the power polar and Figure of Merit for a thrust sweep in hover at 0 deg shaft tilt angle. In this case, the CAMRAD calculations were carried out using a uniform inflow model with an induced power factor κ=1.15. Figure 23 shows the correlations for rotor performance and for the rotor control angles for an advance ratio sweep at C_T/σ = 0.071 and forward shaft tilt of 10 deg. The validation in forward flight was done using a free vortex wake model with tip vortex roll-up using a Scully vorticity distribution and constant core radius. The near wake was truncated at 45 deg azimuth, and dynamic stall was not modeled.

Hover and forward flight performance predictions (see Figures 22 and 23) showed excellent agreement with the measurements. While longitudinal cyclic pitch angles also showed excellent agreement for all advance ratios, collective pitch and lateral cyclic were underpredicted by up to 1 deg for advance ratios of 0.3 and higher.

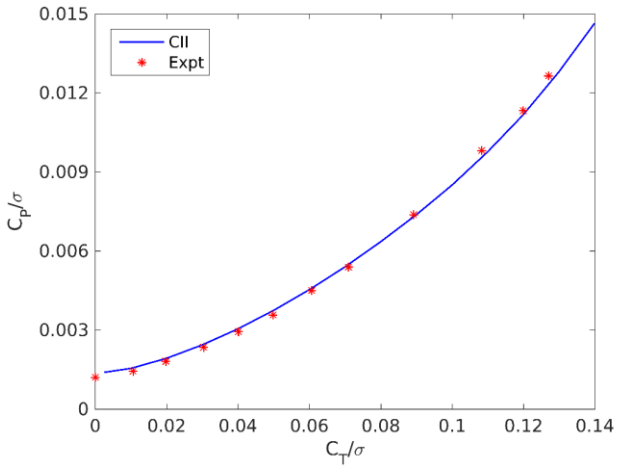

(a) Power polar

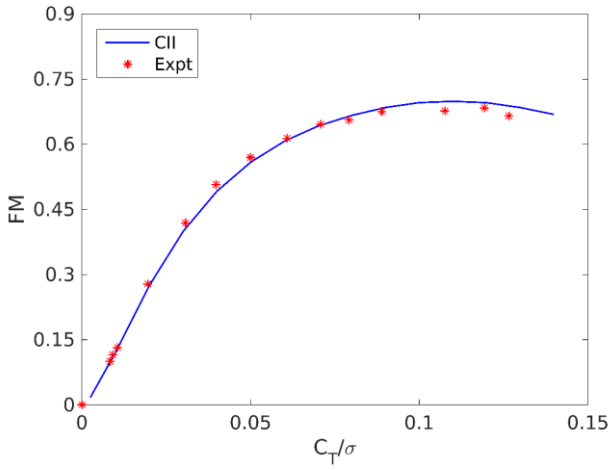

(b) Figure of Merit varying with rotor thrust

Figure 22. Hover performance correlation between experimental results and CAMRAD II (CII) calculations.

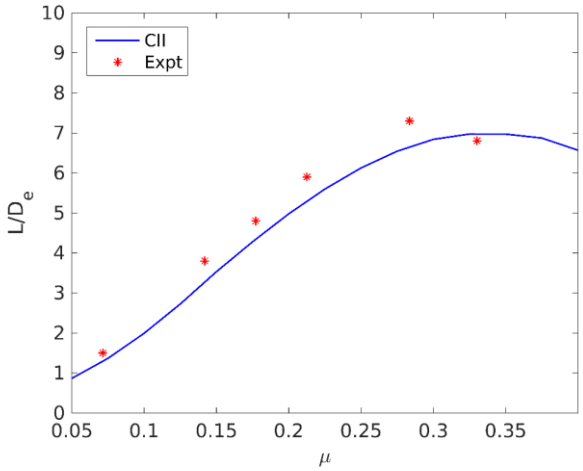

(a) Lift-to-effective-drag ratio

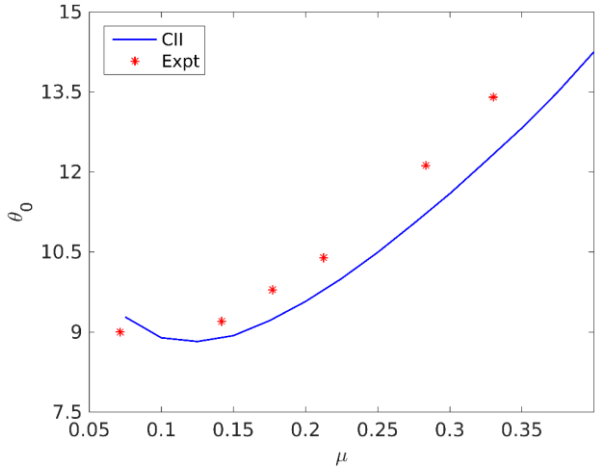

(b) Collective

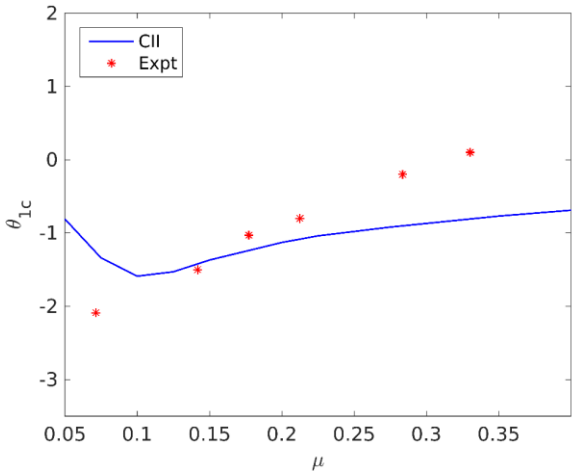

(c) Lateral cyclic

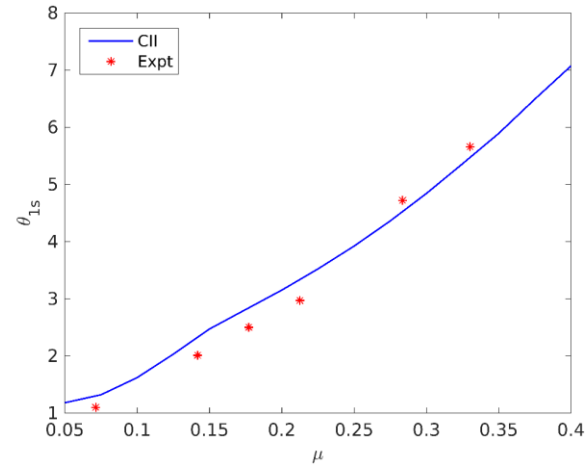

(d) Longitudinal cylic

Figure 23. Forward flight performance and control angle correlations between experimental results and CAMRADII (CII) calculations.

Using this analytical model, a parametric study was conducted to investigate the impact of camber morphing on the performance of the BO-105 full-scale rotor. Figures 24 and 25 show hover results for a static camber change using different deflections of the actuating cambered section, i.e., the different morphed camber shapes (MCCs) that were described previously in this section.

In Figure 24 the Figure of Merit for different static camber morphed cases (i.e., camber deflections) and for different radial positions and length of the camber morphed section are compared to the baseline case. Figure 25 shows the corresponding induced elastic twist. Outboard locations of the morphed section induced greater twist because these sections are much more aerodynamically loaded compared to the inboard sections. Of particular note are the hover performance gains compared to the baseline rotor evident at high C_T/σ for a morphing section of 0.2R radial length; see Figure 24(a). For low to medium thrust, improvement in the Figure of Merit was insignificant. For the smaller morphed sections of 0.05R radial length, gains in FM could be seen only at high blade loadings, albeit to a lesser degree when compared to the longer morphed sections.

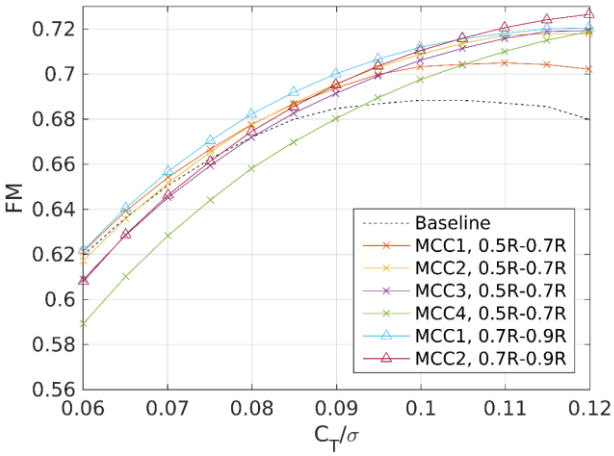

(a) 0.2R morphed camber radial section

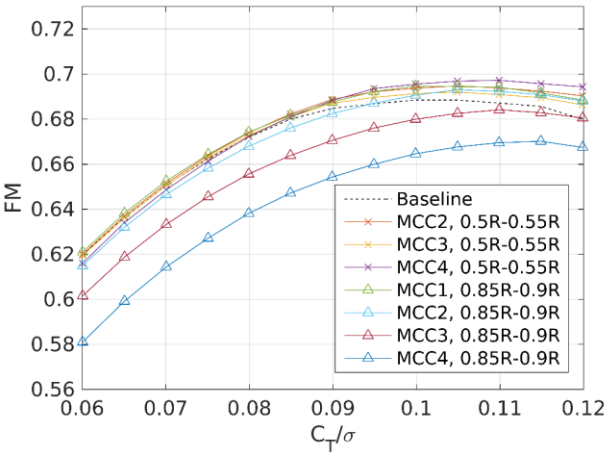

(b) 0.05R morphed camber radial section

Figure 24. Effect of static camber change on hover performance for different radial locations of morphed sections and for long (a) and short (b) morphed sections.

The position of the camber morphing section influenced not only the amount of induced twist, but also its radial distribution over the rotor blade. This is because sections outboard of the actively cambered section are not affected by the induced moment. Furthermore, high induced twist does not necessarily translate to an improved Figure of Merit. For example, in Figure 25(b) an outboard morphing section with the greatest deflection (i.e., MCC4 in this case) produced the highest induced twist but resulted in a lower Figure of Merit. While the 2-D sectional aerodynamics of MCC4 were previously shown to be far inferior to those obtained using the other, less cambered shapes (see Figure 20), the rotor performance could potentially be further degraded by

negative lift on the blade tips induced by very high blade twist (discussed later).

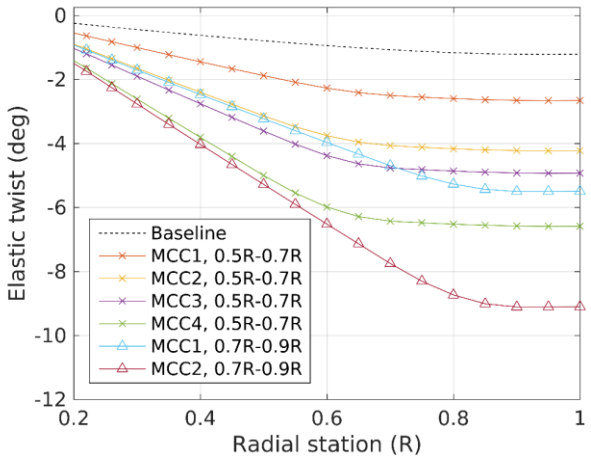

(a) 0.2*R* morphed camber radial section

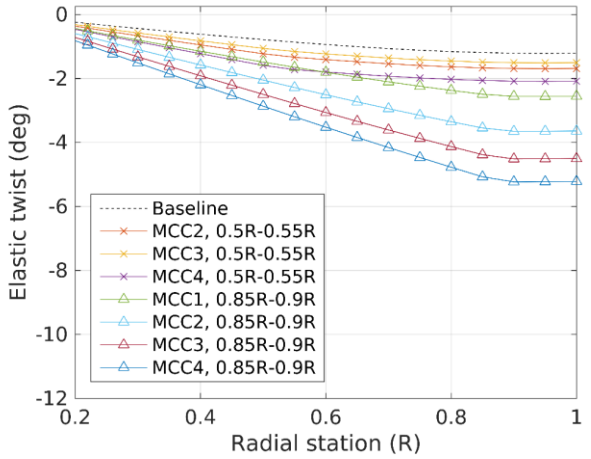

(b) 0.05*R* morphed camber radial section

Figure 25. Effect of static camber change on blade twist in hover, for different radial locations of morphed sections

A high-advance-ratio case (μ=0.313) was investigated for different blade loading coefficients, C_T/σ =0.071, 0.10, and 0.12, a forward shaft tilt of 9.6 deg, and prescribed hub moments in pitch and roll direction of magnitudes 1123 Nm and 1547 Nm, respectively. A dynamic camber morphing actuation at a frequency of 2/rev was implemented with the objective of alleviating uneven disk loadings or lift distributions over the rotor disk that occur in forward flight, and to avoid negative loading (e.g., on the blade tips) as much as possible, thereby reducing the power required for a certain rotor operating condition.

Figure 26 shows the power requirements for varying control phase angles of camber actuation. Both inboard (0.5*R*-0.7*R*) and outboard (0.7*R*-0.9*R*) radial stations were investigated for different blade loading coefficients. The rotor power, C_P, using camber morphing is compared to that required for the baseline rotor, $C_{P,BL}$. The 0 deg phase angle of camber actuation refers to the maximum positive deflection of the actively cambered section occurring at 0 deg of rotor azimuth, ψ. A peak-to-peak camber actuation between the baseline NACA23012 airfoil and the camber morphed profile MCC1 shows increasing performance gains towards higher blade loadings, with a maximum performance gain of 5%. The maximum gain was achieved for C_T/σ =0.12 and for an inboard location of the morphing section; see Figure 26(a). This maximum occurred at a phase angle of 0 deg. Outboard morphing sections either yielded a performance penalty, or the gains in performance were lower than in the case of an inboard morphed section.

Increasing the actuation amplitude retained slightly reduced performance gains of 1-3%, but only for morphing sections located at the inboard stations; see Figure 26(b). Likewise, no considerable gains in performance were obtained for a peak-to-peak camber actuation including negative cambered profile shapes, actuated between NMCC0.5 and MCC0.5; see Figure 26(c). Finally, Figure 26(d) shows results for camber morphing actuation from baseline to MCC0.5, which corresponds to a reduced amplitude compared to all previous cases. The range of phase angles was narrowed to focus on the scheduling where the highest performance gains were induced. The analysis yielded a significant improvement for outboard morphing sections, and even outperformed corresponding morphing cases that were shown in Figure 26(a). Moreover, deviations from the optimum phasing showed less significant performance deterioration for smaller camber deflections than for greater deflections, which is a desirable behavior. With inboard active camber cases, reduced gains were obtained compared to corresponding inboard morphing cases for the same thrust levels, that were previously shown in Figure 26(a).

The amount of camber morphing that resulted in the greatest performance gains was very sensitive to the radial location of the morphing section; see Figure 26 for 0.2*R* morphed segments. For the investigated cases, different radial stations of the camber morphing mechanism required different magnitudes of the 2/rev actuation for obtaining best performance. In general, further inboard placement was more favorable with greater magnitudes of deflection compared to the outer radial stations (that favored less deflection). While inboard the best performing deflection was smaller than MCC2, for outer radial stations camber morphing smaller than MCC1 showed best results. Furthermore, the inboard station of the camber morphing mechanism performed better than outboard in most of the cases. MCC1 inboard actuation yielded best overall performance of the investigated cases (for C_T/σ =0.12), while negative deflections did not show any performance gains in the current study. Best phasing was obtained between -22.5 deg and 0 deg (i.e, greatest deflection occurring between 0 deg rotor azimuth and 22.5 deg before it), depending on the investigated camber case.

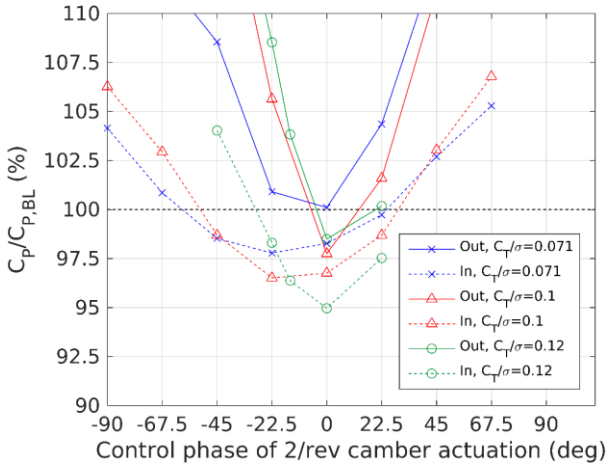

(a) Peak-top-peak camber actuation from baseline to MCC1

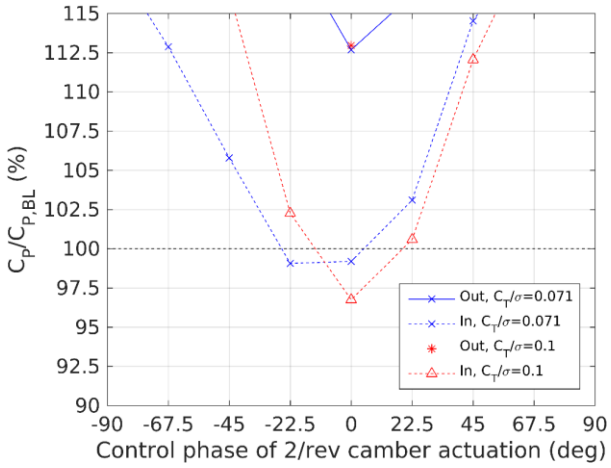

(b) Peak-to-peak camber actuation from baseline to MCC2

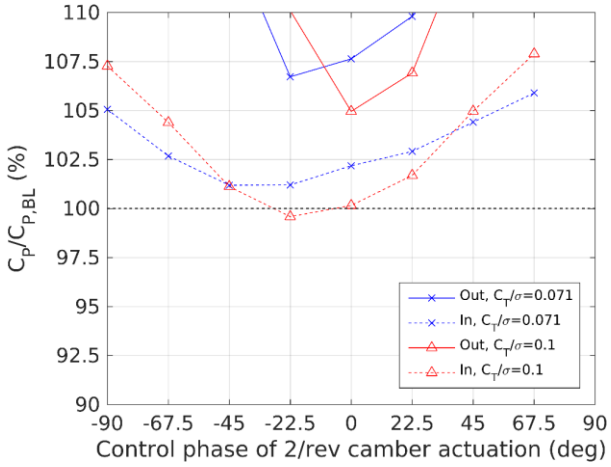

(c) Peak-to-peak camber actuation from NMCC0.5 to MCC0.5

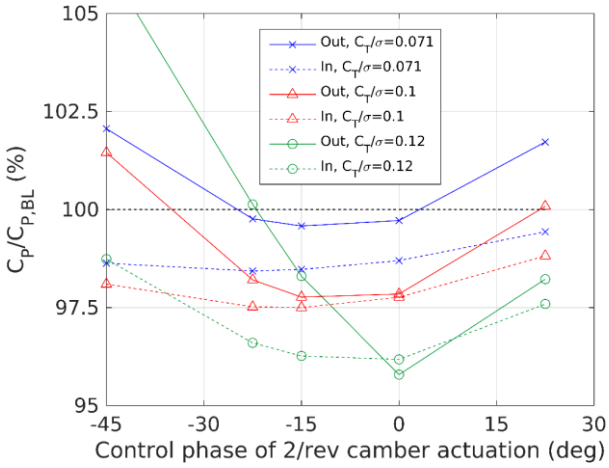

(d) Peak-to-peak camber actuation from baseline to MCC0.5

Figure 26. Effect of phase angle sweep on rotor performance with dynamic camber morphing at 2/rev actuation for different morphing at inboard ('In') and outboard ('Out') radial stations.

To gain further insight into the impact of 2/rev camber morphing on rotor performance, the thrust distribution over the rotor disk was analyzed. A 0 deg phase delay camber actuation was investigated, because it showed the most promising results for the high-speed forward flight trim condition (prescribed hub moments); shown previously in Figure 26 for C_T/σ=0.1. Figures 27 and 28 show plots of thrust distribution over the rotor disk for outboard and inboard location of 0.*2R* camber morphing sections, respectively. Each figure shows the thrust distribution over the baseline rotor disk first and compares it to the thrust distribution obtained for the smallest amplitude of deflection (i.e., MCC0.5) and the next greater (max.) morphed deflection that was studied (i.e., MCC1).

Figure 27(a) shows that the blades were negatively loaded close to the tip on the advancing side. This was alleviated when a 2/rev camber morphing was imposed with a peak-to-peak actuation between the baseline and MCC0.5 (Figure 27(b)), and it completely disappeared when increasing the amplitude of camber morphing to MCC1; see Figure 27(c). This is because maximum positive camber deflection at 0 deg and 180 deg azimuthal positions induced high blade twist in these regions. That has the effect of reducing section angles of attack at the blade outboard stations in the fore and aft regions of the rotor disk. Given the 2/rev actuation of camber morphing adopted here, the 90° and 270° azimuth stations remained unaffected, because the minimum camber deflection in this case was equivalent to the baseline (unmorphed) airfoil. The increase in rotor collective, necessitated by offloading the fore and aft regions of the disk, therefore, increased the disk loading on the advancing and retreating sides. This was more evident for MCC1 (i.e., the greater deflection) than for MCC0.5, because the induced

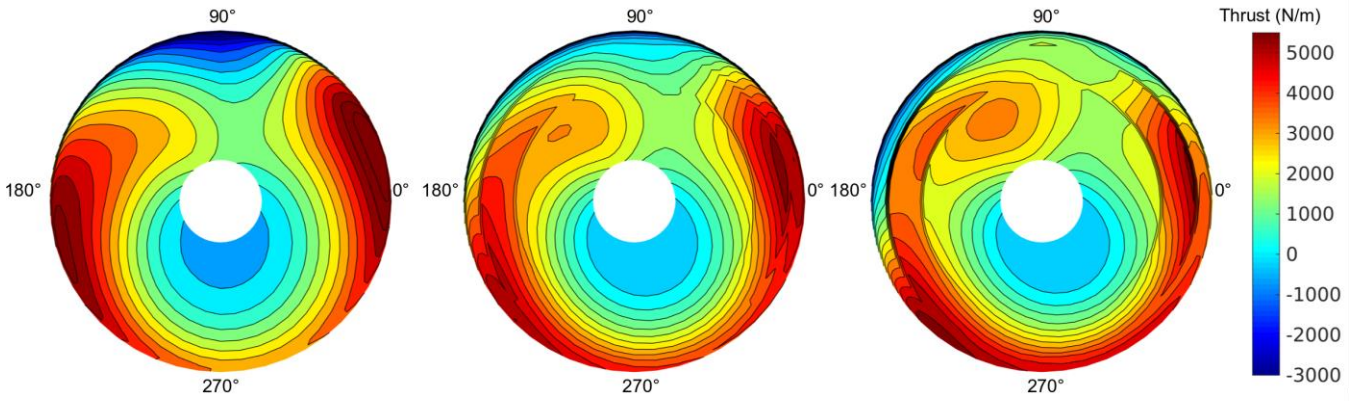

(a) Baseline (b) MCC0.5 (c) MCC1

Figure 27. Thrust distribution for 2/rev actuation of camber morphing section 0.7R-0.9R at C_T/σ =0.1

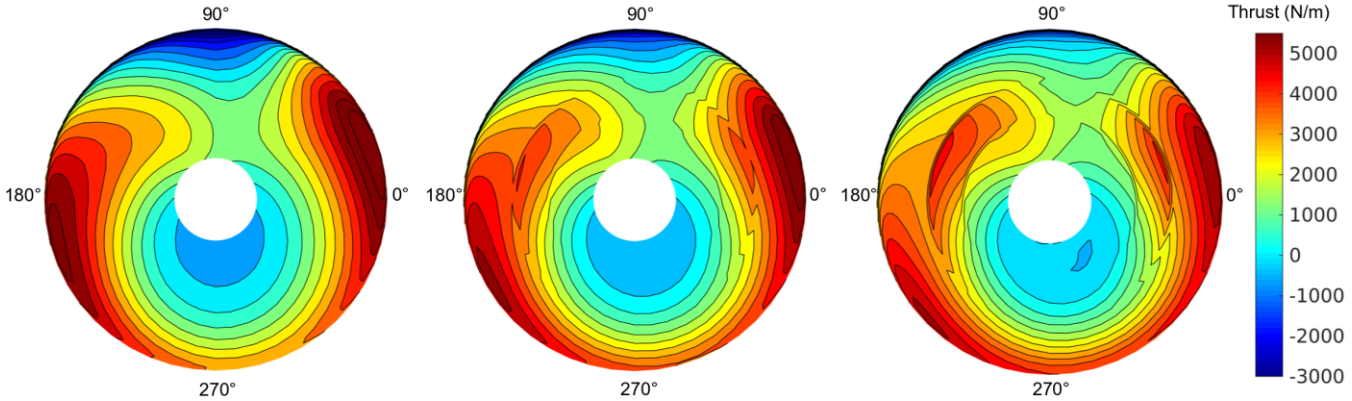

(a) Baseline (b) MCC0.5 (c) MCC1

Figure 28. Thrust distribution for 2/rev actuation of camber morphing section 0.5R-0.7R at C_T/σ =0.1

twist and the correction in collective to achieve the thrust trim target were greater in this case. Furthermore, the high induced twist resulted in a slightly negatively loaded region in the 150 deg to 180 deg azimuthal range; see Figure 27(c), which was not expected to be beneficial for the performance. This condition may also explain the presence of an upper limit of deflection for gaining best performance, which was shown previously in Figure 26.

The inboard positioning of the morphed camber section (see Figure 28) showed a similar trend as previously discussed for the outboard station, although the induced twist magnitudes were less for the inboard flap. The reason for the lower induced twist magnitudes was previously discussed for the hover case; see Figure 25. Therefore, the magnitude of negative thrust on the advancing side as well as the high thrust in the fore and aft regions decreased less significantly compared to the outboard case. However, the thrust in the region of positive camber actuation shifted considerably inboard, because positive cambered airfoils lead to higher lift compared to the baseline profile for the same angle of attack; see Figure 19. In consequence, a beneficial, more even spanwise distribution of thrust was observed. This may be the reason why the inboard position showed generally better performance than the outboard position for the investigated cases (see Figure 26(a)), although it also heavily depended on the C_T/σ combined with the magnitude of camber deflection (compare, e.g., to Figure 26(d)).

PRELIMINARY STUDIES OF ACTIVE TENDONS

This section presents a preliminary analysis of the introduced concept, highlighting its benefits and potential, as well as future challenges that will have to be addressed. Since the experimental studies have not yet been conducted, all presented results have been obtained using numerical low-fidelity modeling. For the numerical model of the baseline BO-105 rotor, the Houbolt-Brooks equations (Ref. 20) (Euler-Bernoulli theory) have been used and the tendon was modeled as a taut string which is rigidly attached to the blade at the tip and passes through the whole body of the blade to the rotor hub where an actuator controls its tension. Although the geometrical and material properties of the tendon are important design variables, their final optimal values have not

yet been determined. Therefore, the following preliminary results are obtained for a nylon rope which is currently seen as one of the candidates to meet material requirements that must be eventually met by the tendon. A set of coupled partial differential equations and corresponding boundary conditions describing the blade with the incorporated tendon was numerically solved by a collocation method to determine the modal properties (natural frequencies and mode shapes) of the system.

The comparison of baseline and modified frequency diagrams can be seen in Figure 29(a). The grey loci represent the response of the baseline rotor with nominal parameters where the first ten modes are considered, and the rotor speed is varied between 0 and 1.2 of the reference (nominal) rotor speed. The modified loci are color-coded according to the dominant mode – the blue solid parts of loci represent the modes dominated by the motion of the blade, the red dashed parts the modes of the tendon, and the green dotted lines mark the veering regions between these two sets of modes. All new loci are related to modes that are dominated by the motion of the tendon and do not therefore have a significant influence on the blade dynamics. The tendon does however influence the blade-dominated modes by reducing their frequency. This tendon-induced reduction is a key effect of the tendon that can be used to control the dynamic behaviour of the blade based on the rotor speed and flying conditions. Moreover, it is necessary to actively control the tendon tension, hence the name "active tendon", in order to overcome the effect of the centrifugal force on the tendon. Without the control, the tendon-induced axial load could cause stability issues at the low rotor speeds while having little effect at operational one. Such a situation is depicted in Figure 29(a) as well. While the reduction of the first blade-dominated mode at the reference rotor speed was relatively minor, the same tendon tension led to a complete disappearance of the first mode at very low rotor speed (highlighted by the purple area in Figure 29(a)).

The dependence of the relative frequency reduction at the reference rotor speed with respect to the modified frequencies on the applied tension and the position of the tendon in the blade is shown in Figure 29(b). The reference value of the tension used to normalize the x-axis is equal to the value for which the modified frequency diagram in Figure 29(b) was computed. Three different tendon positions have been considered. The tendon lies either on the mass axis, elastic axis or behind the elastic axis. It is evident that by increasing the tension the frequency reduction is increased as well. The position of the tendon has also a considerable effect, particularly on the torsional mode. While the frequency of this mode reduces linearly when the tendon coincides with the mass axis, the reduction is approximately quadratic when the tendon lies elsewhere. Therefore, to achieve the optimal performance of the concept, not only the tendon tension must be controlled, but also the position of the tendon in the airfoil must be considered.

From the preliminary analysis shown here, it can be concluded that (a) the tendon can provide a means of reducing

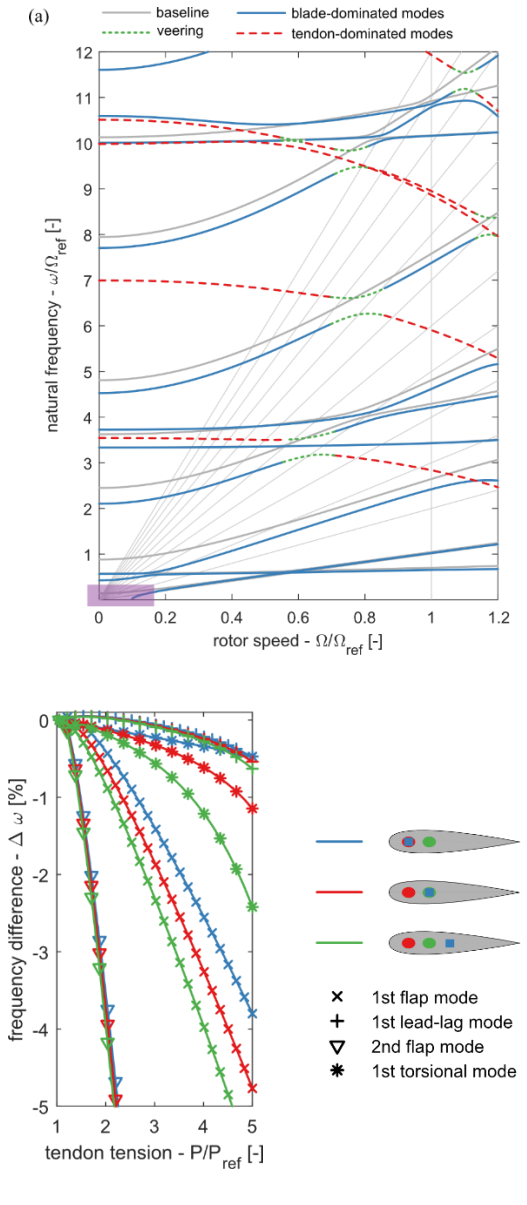

Figure 29. (a) Comparison of the baseline and modified frequency diagrams, and (b) relative reduction with respect to modified frequencies from part (a) of first four natural frequencies of blade-dominated modes at reference rotor speed due to tendon tension and its position within the blade. Position of tendon indicated in legend using a blue square, whereas the mass and elastic axes are represented by the red and green circles, respectively.

the natural frequencies of the blade-dominated modes, (b) the control of the tension must be used to avoid not only potentially harmful resonances, but also stability issues related to the tendon and (c) the position in the tendon in the airfoil should be considered as a design variable. Although the presented preliminary results are encouraging, much work, such as a thorough consideration of stability issues and

experimental validation of the concept, needs to be conducted before the concept can be commissioned.

CONCLUSIONS

Several active rotor morphing concepts were developed, analyzed and tested within a European research program on shape adaptive blades for rotorcraft efficiency (SABRE). In this paper, potential performance improvements were studied of active camber, chord extension, twist, and tendon morphing technologies compared to a baseline BO-105 main rotor.

Initial modeling results of the active tendon concept showed the capabilities of this morphing concept to change the dynamic response of the rotor blade. The results highlighted the potential of the active tendon to provide a means of control required to adaptively avoid harmful resonances at different operational conditions. This can enable rotorcraft to operate over a wider range of rotor speeds, thereby increasing their efficiency and decreasing fuel burn, air pollution and noise emission.

2D aerodynamics results showed promising airfoil performance gains for the studied active camber mechanisms. Likewise, a BEMT analysis and optimization showed that significant rotor performance gains can be achieved by the proposed active chord extension including deflection, by active twist, and combinations thereof. It was found that the most efficient combination of these morphing parameters was 100% extended chord (doubling the solidity at the root) with and without deflection of the extended chord section and overlaid by -8 deg/R of additional morphed twist, yielding rotor hover power reductions of up to 11% for high-thrust conditions.

The lower-order modeling results and the 2D CFD results were incorporated into full-scale rotor comprehensive analysis models that were developed using CAMRAD II. The analytical model of the baseline BO-105 main rotor was validated using full-scale rotor measurements that were previously conducted by NASA in the 40-by-80-ft wind tunnel at NASA Ames Research Center. Predictions were made of the performance gains to be expected using the active camber morphing mechanisms integrated into a BO-105 main rotor blade when compared to the baseline BO-105 rotor. Small positive camber morphing at 2/rev actuation of the aft quarter chord of the airfoil section showed encouraging results for a high-speed forward flight case at an advance ratio of 0.313.

Performance gains were found to be heavily dependent on active camber section placement and deflection, length of the morphed section, rotor blade loading coefficient, and actuation control phasing. Initial studies on the active camber morphing showed gains in hover Figure of Merit of up to 5.5% (static morphing), and up to 5% in forward flight when dynamically actuated at 2/rev. The 5% performance gain in forward flight was achieved by a 0.2R morphed camber section located at 0.5-0.7R. These rotor efficiency gains were partly effected by induced elastic twist that redistributed the rotor disk loading more uniformly, and also by the morphed cambered sections showing better airfoil efficiency than the baseline NACA23012 airfoil.

These initial results from lower-order modeling will inform morphing technology development with respect to deflection targets, geometric placement of the mechanisms on the blades, expected operational conditions, etc. Using these initial results from sweeps of the design space and operating range, any further more refined analysis models (also using higher-order aerodynamics) can focus on a sub-space of parameters, hence decreasing the computational effort, to further investigate rotor performance using the discussed morphing technologies.

Author contact:

Jürgen Rauleder: juergen.rauleder@tum.de

Berend G. van der Wall: berend.vanderwall@dlr.de

Amine Abdelmoula: amine.abdelmoula@tum.de

Dominik Komp: dominik.komp@tum.de

Sumeet Kumar: sumeet.kumar@tum.de

Vaclav Ondra: vaclav.ondra@bristol.ac.uk,

Brano Titurus: brano.titurus@bristol.ac.uk,

Benjamin Woods: ben.k.s.woods@bristol.ac.uk

ACKNOWLEDGMENTS

This project has received funding from the European Union's Horizon 2020 research and innovation program under grant agreement No. 723491.

REFERENCES

[1] Yeo, H., "Assessment of Active Controls for Rotor Performance Enhancement," *Journal of the American Helicopter Society*, Vol. 53, (2), Apr. 2008, pp. 152–163.

[2] Yeo, H., Romander, E. A., and Norman, T. R., "Investigation of Rotor Performance and Loads of a UH-60A Individual Blade Control System," *Journal of the American Helicopter Society*, Vol. 56, Oct. 2011, pp. 1–18.

[3] Woods, B. K., and Friswell, M. I., "Spiral pulley negative stiffness mechanism for passive energy balancing," *Journal of Intelligent Material Systems and Structures*, Vol. 27, (12), Aug. 2015, pp. 1673-1686.

[4] *FRIENDCOPTER: Integration of technologies in support of a passenger and environmentally friendly helicopter*.

[5] Woods, B. K. S., and Friswell, M. I., “Preliminary Investigation of a Fishbone Active Camber Concept,” Proceedings of the ASME 2012 Conference on Smart Materials, Adaptive Structures and Intelligent Systems, Stone Mountain, GA, Sept. 19-21, 2012.

[6] Woods, B. K. S., Bilgen, O., and Friswell, M. I., “Wind tunnel testing of the Fish Bone Active Camber morphing concept,” *Journal of Intelligent Material Systems and Structures*, Vol. 25, Feb. 2014.

[7] Werter, N., Sodja, J., Spirlet, G., and Breuker, R. D., “Design and Experiments of a Warp Induced Camber and Twist Morphing Leading and Trailing Edge Device,” 24th AIAA/AHS Adaptive Structures Conference, San Diego, CA, Jan 4-8, 2016.

[8] Bubert, E. A., Woods, B. K. S., Lee, K., Kothera, C. S., and Wereley, N. M., “Design and Fabrication of a Passive 1D Morphing Aircraft Skin,” *Journal of Intelligent Material Systems and Structures*, Vol. 21, Nov. 2010, pp. 1699–1717.

[9] Du Bois, J. L., Lieven, N. A., and Adhikari, S., “Adaptive Passive Control of Dynamic Response Through Structural Loading,” Paper AIAA 2007-2221, 48th AIAA/ASME/ASCE/AHS/ASC Structures, Structural Dynamics, and Materials Conference, Apr. 23-26, 2007.

[10] Turkstra, T. P., and Semercigil, S. E., “Elimination of resonance with a switching tensile support,” *Journal of Sound and Vibration*, Vol. 163, 1993, pp. 359–362.

[11] Virgin, L. N., and Plaut, R. H., “Effect of Axial Load on Forced Vibrations of Beams,” *Journal of Sound and Vibration*, Vol. 168, Dec. 1993, pp. 395–405.

[12] Dibble, R., and Titurus, B., “Helicopter rotor blade modal tuning using internal preloads,” ISMA 2016 International Conference on Noise and Vibration Engineering, Leuven, 2016.

[13] Johnson, W., "Technology Drivers in the Development of CAMRAD II," American Helicopter Society Aeromechanics Specialists Conference, San Francisco, CA, January 19–21, 1994.

[14] M. Drela, "XFOIL: An analysis and design system for low Reynolds number airfoils," Lecture Notes in Engineering, Vol. 54, Springer Verlag, 1989.

[15] Woods, B. K. S., Fincham, J. H. S., and Friswell M. I., "Aerodynamic modelling of the fish bone active camber morphing concept," Proceedings of the RAeS Applied Aerodynamics Conference, Bristol, UK. Vol. 2224, 2014.

[16] Althaus, D., and Wortmann, F. X., "Stuttgarter Profilkatalog: Messergebnisse aus dem Laminarwindkanal des Instituts für Aerodynamik und Gasdynamik der Universität Stuttgart," F. Vieweg, 1981.

[17] "Bo105: Configuration Data," WP-10 Report GARTEUR HC AG 16, 2006.

[18] Peterson, R. L., Maier, T., Langer, H. J., and Trainapp, N., "Correlation of Wind Tunnel and Flight Test Results of a Full-Scale Hingeless Rotor," Proceedings of the American Helicopter Society Aeromechanics Specialist Conference, San Francisco, CA, 1994.

[19] Peterson, R. L., "Full-Scale Hingeless Rotor Performance and Loads," NASA TM 110356, June 1995.

[20] Houbolt, J. C., and Brooks, G. W., "Differential equations of motion for combined flapwise bending, chordwise bending, and torsion of twisted nonuniform rotor blades," NACA TN 3905, Feb. 1957.